Clairvoyant Radar Sea Clutter Covariance Matrix Modelling

Michael Kenneth McDonald and Delphine Cerutti-Maori, *Senior member IEEE*

Abstract

Closed form expressions are derived for the calculation of the clairvoyant covariance matrix for radar sea clutter arising from individual clutter components with Gaussian spectra. Two forms are presented corresponding to a power series expansion of a sinc^2 antenna gain pattern and a Gaussian approximation to the mainlobe of the antenna pattern. The variation of covariance matrix eigenvalues due to factors such as coherent pulse interval (CPI), spectra bandwidth, centre frequency and relative power is examined.

Index Terms

Radar, sea clutter, covariance matrix.

I. Introduction

Sea clutter spectra are frequently modelled as arising from the addition of clutter spectra associated with backscatter from different sea surface clutter mechanisms. Commonly these clutter mechanisms are described as slow and fast scatterers due to the different Doppler velocity shifts they exhibit. Slow clutter is believed to arise primarily due to Bragg scattering from capillary waves while fast scatter arises through backscatter from gravity wave phenomena such as wave breaking. These component spectra are frequently modelled assuming Gaussian shaped spectral components, see for instance [1]–[4].

The assumption of Gaussian shaped spectra for different components is exploited below to derive closed form expressions for covariance matrices collected from radars mounted on moving platforms. As discussed by McDonald and Cerutti-Maori [5], [6] the different clutter component mechanisms are usefully considered as statistically independent. This allows for the covariance matrices to be individually derived and added to form the overall composite matrix. By appropriately scaling and frequency shifting of the individual Gaussian spectra, a range of arbitrary overall clutter spectra can be closely replicated.

The goals of this analysis are two fold: 1) to provide a closed form model for the clairvoyant covariance matrix corresponding to an observed mean spectral response which in turn supports eff cient generation of simulated data,

M. McDonald is with Defence Research & Development Canada Ottawa Research Centre (DORC), 3701 Carling Avenue, Ottawa, ON, Canada. e-mail: mike.mcdonald@drdc-rddc.gc.ca

D. Cerutti-Maori is with the Fraunhofer Institute for High Frequency Physics and Radar Techniques (FHR) in Wachtberg, Germany.

and 2) utilise this model to provide insights into observed departures of sea clutter eigenspectra from that observed for ground clutter observations. The results provide insights into the physical meaning of the observed behaviour which assists ongoing efforts to adapt ground moving target indication (GMTI) space time adaptive processing (STAP) methodologies to maritime moving target detection [5]–[9].

II. Covariance matrix calculation for sinc^2 antenna pattern

The derivation of the single Gaussian spectral component covariance matrix commences with the following straightforward definition for the deterministic part of a single channel clutter backscatter signal, $s_t(\theta, \omega_c)$ at slow time t for a given azimuth angle θ and specified clutter inherent angular Doppler velocity, ω_c,

$$s_t(\theta, \omega_c) = A(\theta) e^{\jmath \omega_A(\theta) t} \sqrt{g(\omega_c, \omega_m)} e^{\jmath \omega_c t}, \tag{1}$$

where θ is the azimuth angle of arrival, $g(\omega_c)$ specifies the form of the inherent Gaussian spectrum of the clutter and $A(\theta)$ specifies antenna azimuth amplitude gain. $\omega_A(\theta)$ corresponds to the apparent Doppler shift that is imparted to an infinitesimal clutter patch at angle θ in the antenna beam pattern due to the movement of the platform. To clarify, the subsequent use of the term inherent angular Doppler frequency or inherent Doppler frequency refers to the Doppler frequency that would be measured for the clutter contribution if the radar were not moving. Furthermore, the term Doppler velocity is used to describe the velocity a reflecting object would have to possess to generate the observed Doppler frequency.

For a broadside viewing geometry the angular Doppler frequency associated with this apparent Doppler velocity can be written as

$$\omega_A(\theta) = \frac{4\pi v_p f_0}{c} \sin(\theta) \widehat{=} Q \sin(\theta), \tag{2}$$

where f_0 denotes the modulation frequency and v_p denotes the platform frequency. c is the speed of light. The above equation, while frequently used, assumes a flat earth geometry. Long range and high grazing angle geometries will introduce some departures from the modelled results.

As discussed above the clutter is assumed to have a Gaussian power spectrum yielding

$$g(\omega_c, \omega_m) = \frac{1}{\sigma_c \sqrt{2\pi}} e^{-\frac{(\omega_c - \omega_m)^2}{2\sigma_c^2}}, \tag{3}$$

where ω_m specifies the centre frequency of the spectrum and σ_c specifies its width. The total power has been arbitrarily normalised to 1.

For a system in which s_t is measured at discrete, equally spaced values of t, we can form a $N \times 1$ vector $\mathbf{t} = [t_1, t_2, ..., t_N]^T$, where N is the total number of measurements within a coherent processing interval (CPI) and $\delta t = t_{n+1} - t_n$. The received signal vector can be written as

$$\mathbf{S_t}(\theta) = \begin{bmatrix} s_{t_1}(\theta, \omega_c) \\ s_{t_2}(\theta, \omega_c) \\ \vdots \\ s_{t_N}(\theta, \omega_c) \end{bmatrix}. \tag{4}$$

The expression for the $N \times N$ covariance matrix, $\mathbf{R_t}(\theta, \omega_c)$ corresponding to a single inherent frequency from the clutter patch at θ is now given by

$$\mathbf{R_t}(\theta,\omega_c) = \mathbf{S_t}(\theta)\mathbf{S_t}^H(\theta) = A^2(\theta)g(\omega_c,\omega_m) \begin{bmatrix} e^{\jmath t_1(\omega_A(\theta)+\omega_c)} \\ e^{\jmath t_2(\omega_A(\theta)+\omega_c)} \\ \vdots \\ e^{\jmath t_N(\omega_A(\theta)+\omega_c)} \end{bmatrix} \begin{bmatrix} e^{\jmath t_1(\omega_A(\theta)+\omega_c)} \\ e^{\jmath t_2(\omega_A(\theta)+\omega_c)} \\ \vdots \\ e^{\jmath t_N(\omega_A(\theta)+\omega_c)} \end{bmatrix}^H . \tag{5}$$

The above expression will be integrated across ω_c to incorporate the contribution from all inherent clutter components. In anticipation of this step the following substitution, $\omega = \omega_c - \omega_m$, is made to the variable of integration yielding

$$g(\omega) = \frac{1}{\sigma_c\sqrt{2\pi}} e^{-\frac{\omega^2}{2\sigma_c^2}}. \tag{6}$$

The full inherent spectrum covariance matrix for the clutter patch at θ is now given by integrating each element of the covariance matrix

$$\mathbf{R_t}(\theta) = \int_{-\infty}^{\infty} \mathbf{R_t}(\theta, \omega + \omega_m) d\omega, \tag{7}$$

where $d\omega = d\omega_c$. The form of (7) arises from the assumption that spectral components of the inherent clutter spectrum are statistically independent. This assumption can be justif ed by the realisation that the spectral width typically arises due to backscatter from different locations within the measurement cell and from different surface features. For example, the Bragg spectral width is effectively modelled as arising from capillary wave scattering located at different locations on the gravity wave structure [10].

Using the following integral identity known as the Hubbard−Stratonovich transformation

$$\int_{-\infty}^{\infty} e^{-ax^2} e^{-bx} dx = \sqrt{\frac{\pi}{a}} e^{\frac{b^2}{4a}} \tag{8}$$

each element, $\mathbf{R_{t}}_{i,k}(\theta)$ can then be written as

$$\mathbf{R_{t}}_{i,k}(\theta) = A^2(\theta) c_{i,k} e^{\jmath(\omega_A(\theta)+\omega_m)(i-k)\delta t} \tag{9}$$

where $c_{i,k} = e^{-(i-k)^2\delta t^2(\sigma_c^2/2)}$.

The development so far has been limited to the response from a single antenna aperture. The full spatial-temporal covariance matrix, $\mathbf{R_{t,d}}(\theta)$ for a multichannel antenna system with M antenna sub-apertures can be derived as follows

$$\mathbf{R_{t,d}}(\theta) = [\mathbf{S_d}(\theta) \odot \mathbf{S_t}(\theta)] [\mathbf{S_d}(\theta) \odot \mathbf{S_t}(\theta)]^H = \mathbf{S_d}(\theta)\mathbf{S_d}^H(\theta) \odot \mathbf{R_t}(\theta) \tag{10}$$

where $\odot$ denotes the Kronecker operator. The $M \times 1$ spatial vector $\mathbf{S_d}(\theta)$ takes the form

$$\mathbf{S_d}(\theta) = \left[e^{-\jmath\frac{2\pi d}{\lambda}(m-1)\sin(\theta)} \right]_{m=1}^{M}. \tag{11}$$

The transmitted signal wavelength is $\lambda = \frac{c}{f_0}$. The resulting covariance matrix $\mathbf{R}_{\mathbf{t},\mathbf{d}}(\theta)$ has dimensions $MN \times MN$ and has the block diagonal form as follows

$$\mathbf{R}_{\mathbf{t},\mathbf{d}}(\theta) = \begin{array}{c} \\ I{=}1 \\ I{=}2 \\ \vdots \\ I = M \end{array} \begin{array}{c} \begin{array}{cccc} K{=}1 & K{=}2 & \cdots & K = M \end{array} \\ \begin{bmatrix} \mathbf{R}_{\mathbf{t}}(\theta) & e^{-\jmath C_D \sin(\theta)}\mathbf{R}_{\mathbf{t}}(\theta) & \cdots & e^{-\jmath(M-1)C_D \sin(\theta)}\mathbf{R}_{\mathbf{t}}(\theta) \\ e^{\jmath C_D \sin(\theta)}\mathbf{R}_{\mathbf{t}}(\theta) & \mathbf{R}_{\mathbf{t}}(\theta) & \ddots & \vdots \\ \vdots & \ddots & \ddots & e^{-\jmath C_D \sin(\theta)}\mathbf{R}_{\mathbf{t}}(\theta) \\ e^{\jmath(M-1)C_D \sin(\theta)}\mathbf{R}_{\mathbf{t}}(\theta) & \cdots & e^{\jmath C_D \sin(\theta)}\mathbf{R}_{\mathbf{t}}(\theta) & \mathbf{R}_{\mathbf{t}}(\theta) \end{bmatrix} \end{array} \tag{12}$$

where $C_D = \frac{2\pi d}{\lambda}$. The indexes $I = [1, M]$ and $K = [1, M]$ refers to the block row and column, and the indexes $i = [1, N]$ and $k = [1, N]$ refer to the local row and column within a matrix block.

The elements of $\mathbf{R}_{\mathbf{t},\mathbf{d}}(\theta)$ are now given by

$$\mathbf{R}_{\mathbf{t},\mathbf{d}_{I,K}}(\theta) = e^{\jmath(I-K)C_D \sin(\theta)}\mathbf{R}_{\mathbf{t}}(\theta). \tag{13}$$

The full spatial-temporal covariance matrix can now be calculated by integrating over all θ as follows

$$\mathbf{R}_{\mathbf{t},\mathbf{d}} = \int_{-\infty}^{\infty} \mathbf{R}_{\mathbf{t},\mathbf{d}}(\theta)\mathrm{d}\theta. \tag{14}$$

A similar assumption to that discussed for equation 7 is exploited in the formation of equation 14, namely that the integrated components, in this case the clutter backscatter from each azimuth location, are statistically independent due to the fact that they arise from different physical locations. The integration range for θ can be set to $[-\infty, \infty]$ as $\mathbf{R}_{\mathbf{t},\mathbf{d}}(\theta)$ goes to zero outside the range $[-\pi, \pi]$

For a rectangular antenna array transmitting on all apertures and receiving on individual apertures the antenna gain pattern $A(\theta)^2$ is well described by a sinc^2 (i.e., sinc $= \frac{\sin(x)}{x}$) function. Unfortunately the solution of equation 14 is not readily available for the sinc^2 function. To make further progress the power series approximation to sinc^2 is used, i.e.,

$$A^2(\theta) = \mathrm{sinc}^2(\theta) = \sum_{p=1}^{\infty} \frac{2^{2p-1}(-1)^{p-1}\theta^{2(p-1)}}{(2p)!}. \tag{15}$$

Combining equations 13, 14 and 15 and using the approximation $\sin(\theta) \approx \theta$ for small θ leads to an equation of the form

$$\mathbf{R}_{\mathbf{t}_{i,k},\mathbf{d}_{I,K}} = c_{i,k}e^{\jmath\omega_m(i-k)\delta t} \int_{-\infty}^{\infty} e^{\jmath D\theta} \sum_{p=1}^{\infty} \frac{2^{2p-1}(-1)^{p-1}\theta^{2(p-1)}}{(2p)!}\mathrm{d}\theta \tag{16}$$

where $D = C_D(I-K) + Q(i-k)\delta t$. The $\sin(\theta) \approx \theta$ for small θ is applicable for most practical airborne radars systems utilised for maritime surveillance with even broad beamwidths of 30^o (i.e. $+/-15^o$) introducing an error of approximately 1%. Making use of the antiderivative identity

$$\int x^n e^{cx} dx = e^{cx} \sum_{q=0}^{n} \frac{(-1)^q n! x^{n-q}}{(n-q)! c^{q+1}} \tag{17}$$

TABLE I

SYSTEM AND GEOMETRIC PARAMETERS FOR MODELLING AND SIMULATION.

Viewing geometry	Sidelooking looking wrt aircraft motion
Platform velocity (v_p)	100 m/s
Transmit frequency (f_0)	9.09 GHz
Antenna azimuth width	80 cm
Antenna gain pattern FWHM	2.4 deg
Number of channels	3
Antenna phase centre separation (d)	26.6 cm
CPI	64 pulses (64 ms)
Pulse repetition frequency (PRF)	1 kHz

and limiting the range of the integration over dx, equation 17 now takes the form

$$\mathbf{R}_{\mathbf{t}_{i,k},\mathbf{d}_{I,K}} = c_{i,k}e^{\jmath\omega_m(i-k)\delta t}\sum_{p=1}^{\infty}\sum_{q=0}^{2(p-1)} e^{jD\theta}\frac{2^{2p-1}(-1)^{p-1+q}(2(p-1))!\theta^{2(p-1)-q}}{(2p)!(2(p-1)-q)!(jD)^{q+1}}\Bigg|_{\theta_L}^{\theta_U} \tag{18}$$

where $[\theta_L, \theta_U]$ def nes the integration limits. In general abs$(\theta_L) = \theta_U = \delta_\theta$ due to the symmetry of the antenna beam pattern. After some straightforward, if tedious, manipulations equation 18 can be rearranged to yield matrix elements

$$\begin{aligned}\mathbf{R}_{\mathbf{t}_{i,k},\mathbf{d}_{I,K}} = c_{i,k}e^{\jmath\omega_m(i-k)\delta t}&\sum_{\text{pow=0:2:power}}(-1)^{\text{pow}/2}2C_{\text{even}}(\text{pow})(\delta_\theta)^{\text{pow}}\sin(\delta_\theta D)\\ +c_{i,k}e^{\jmath\omega_m(i-k)\delta t}&\sum_{\text{pow=1:3:power}}(-1)^{\text{ceiling}(\text{pow}/2)}2C_{\text{odd}}(\text{pow})(\delta_\theta)^{\text{pow}}\cos(\delta_\theta D)\end{aligned} \tag{19}$$

where 'ceiling' denotes the round up function and

$$C_{\text{even}}(\text{pow}) = \sum_{n=1}^{\frac{\text{power}-\text{pow}}{2}+1}\frac{2^{2n+\text{pow}-1}(2(n-1)+\text{pow})!}{(2(n+\text{pow}/2))!\text{pow}!D^{2n-1}} \tag{20}$$

and

$$C_{\text{odd}}(\text{pow}) = \sum_{n=1}^{\frac{\text{power}}{2}-\text{ceiling}(\frac{\text{power}}{2})+1}\frac{2^{2n+\text{pow}}(2n+\text{pow}-1)!}{(2(n+\text{ceiling}(\text{pow}/2)))!\text{pow}!D^{2n}}. \tag{21}$$

In the above 'power' corresponds to the highest power term that is used for the power series expansion. Figure 1 plots a true sinc^2 function along side 14^{th} and 28^{th} order power series approximations for the sinc^2 function. Table I below summarises a number of system and geometric parameters which are assumed to apply for the various modelled and simulated results presented throughout this paper. It can be seen that while the 14^{th} order result provides a good approximation to the main lobe, a 28^{th} order approximation is required to incorporate the f rst sidelobe. Practically, these very high order approximations are diff cult to calculate due to the accumulation of round off errors. It is important to note that the integration limits, $[\theta_L, \theta_U]$, in equation 18 should be specif ed to only cover the region in which the sinc^2 function is accurately represented.

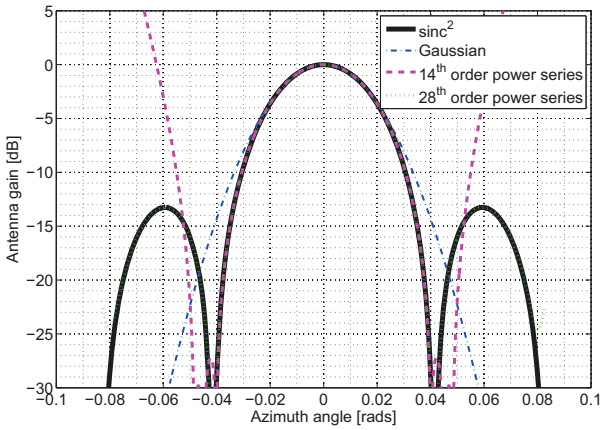

Fig. 1. Comparisons of actual sinc^2 antenna gain pattern with 14^{th} and 28^{th} order power series expansion and Gaussian approximation. sinc^2 and power expansion curves are difficult to visually separate over main lobe (and first sidelobe for 28^{th} order expansion) as they heavily overlap.

In this paper the focus is on results associated with post-Doppler space time adaptive processing (STAP) in which the data measured via individual antenna channels is transformed to the frequency domain, typically via fast fourier transform (FFT). The frequency bins are then treated as statistically independent and adaptation is undertaken on a Doppler bin to Doppler bin basis. Various versions of this approach have been developed, such as pulse repetition interval (PRI)-staggered post-Doppler STAP, but we limit our analysis to factored STAP in which the final adaptation is limited to the spatial (or angular) coordinate. The details of the various sub-optimal STAP processing approaches is beyond the scope of this paper and the interested reader is referred to Ward [11] for a useful overview. For the purposes of the ensuing analysis it is sufficient to understand that it is necessary to extract the $M \times M$ matrix, $\mathbf{R}_{f_d,\mathbf{d}}$ corresponding to a given frequency bin f_d. This is accomplished via the mapping

$$\mathbf{R}_{f_d,\mathbf{d}} = \mathbf{F}(f_d)\mathbf{R}_{\mathbf{t},\mathbf{d}}\mathbf{F}^H(f_d) \tag{22}$$

where $\mathbf{F}(f_d)$ is a $M \times NM$ matrix of the form

$$\mathbf{F}(f_d) = \begin{bmatrix} \mathbf{s}_{f_d} & \mathbf{0} & \cdots & \mathbf{0} \\ \mathbf{0} & \mathbf{s}_{f_d} & \ddots & \vdots \\ \vdots & \mathbf{0} & \ddots & \mathbf{0} \\ \mathbf{0} & \ldots & \mathbf{0} & \mathbf{s}_{f_d} \end{bmatrix} \tag{23}$$

with the $1 \times N$ vector $\mathbf{s}_{f_d} = [1, e^{-\jmath 2\pi f_d \delta t}, \cdots, e^{-\jmath 2\pi f_d \delta t(N-1)}]$.

Figure 2 presents predicted eigenvalues versus Doppler velocity plots for the model using a 14^{th} order approximation (SM1, SM2, SM3) as as well as values derived from simulated data measurements using an actual sinc^2 antenna gain pattern (SS1, SS2, SS3). Excellent agreement is observed between the results across the main lobe as might have been anticipated from figure 1. For all simulations undertaken in this paper the total clutter-to-noise ratio

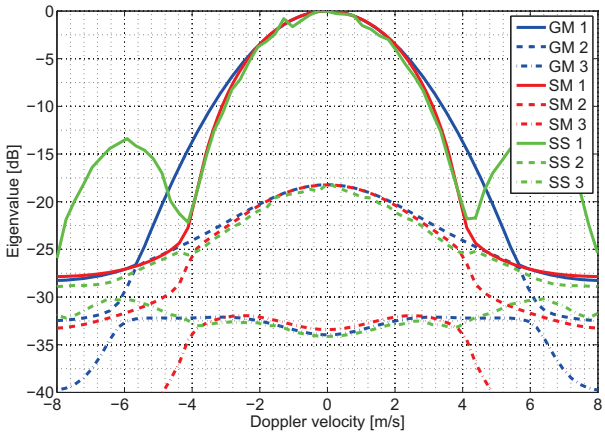

Fig. 2. Eigenvalues spectra from Monte Carlo simulations using sinc^2 antenna patten (SS1, SS2, SS3), 14^{th} order power series approximation model (SM1, SM2, SM3) and Gaussian approximation model (GM1, GM2, GM3).

(CNR) of the signal is intentionally set very high (>60 dB) to minimize the effects of white noise and highlight the effects that are due to clutter alone. The inclusion of noise is straightforward, see equation 28 below, and is not found to signif cantly alter any conclusion or observations that are detailed in this paper. As such the corresponding results are not presented for conciseness.

III. Covariance matrix calculation for Gaussian antenna pattern

Considerable simplif cation can achieved by approximating the main lobe of $A^2(\theta)$ in equation 13 as a Gaussian, i.e.,

$$A(\theta)^2 = \frac{1}{\sigma_\theta\sqrt{2\pi}} e^{-\frac{\theta^2}{2\sigma_\theta^2}}. \tag{24}$$

Equation 13 now takes the form

$$\mathbf{R}_{\mathbf{t}_{i,k},\mathbf{d}_{I,K}}(\theta) = \frac{1}{\sigma_\theta\sqrt{2\pi}} e^{-\frac{\theta^2}{2\sigma_\theta^2}} e^{\jmath(I-K)C_D\sin(\theta)} c_{i,k} e^{\jmath(\omega_A(\theta)+\omega_m)(i-k)\delta t}. \tag{25}$$

Again exploiting the identity of equation 8 and $\sin(x) \approx x$ we obtain the compact expression

$$\mathbf{R}_{\mathbf{t}_{i,k},\mathbf{d}_{I,K}} = c_{i,k} e^{\jmath\omega_m(i-k)\delta t} e^{-\frac{D^2\sigma_\theta^2}{2}} \tag{26}$$

for each element in $\mathbf{R}_{\mathbf{t},\mathbf{d}}$.

Figure 1 plots the resulting antenna gain pattern when the Gaussian is scaled to match its full half width maximum (FHWM) with the FHWM of the sinc^2. It can be seen that Gaussian approximation provides a good match across the central portion of the main lobe but leads to a wider beamwidth in the lower gain regions of the main lobe and, as anticipated, does not model the sidelobes at all. These observations are further ref ected in the eigenvalue spectra for the Gaussian model (GM1, GM2, GM3) plotted in f gure 2, where good agreement with the simulated sinc^2 results is observed only across the central section of the main lobe.

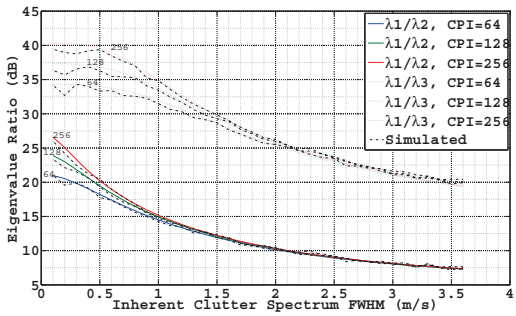

Fig. 3. Ratio of first to second eigenvalues (λ_1/λ_2) and first to third eigenvalues (λ_1/λ_3) as a function of inherent sea clutter FWHM spectral width. Results from Monte Carlo data simulations is shown as a black dot-dash line.

The variation of eigenvalues with changing inherent clutter spectrum width is examined in figure 3 where the ratios of the largest eigenvalue with respect to the second and third eigenvalue are plotted versus inherent spectrum FWHM bandwidth. Details of the observed behaviour were discussed extensively by McDonald and Cerutti-Maori [7], for this paper it is simply noted that the modelling approach accurately captures the strong dependence on CPI lengths that was previously noted for small spectral FWHM. This small FWHM effect can lead to errors for techniques based on Taylor series expansions around the stationary clutter eigenvector [12]. The slight tendency of the simulated results to underestimate modelled results at small FHWM values can be traced to the Gaussian approximation to the antenna beam pattern which tends to produce a slightly narrower spectrum for gain values greater than -3dB. If the Monte Carlo simulations are run using a Gaussian antenna pattern an improved match to model predictions is obtained (not shown for conciseness).

IV. Multi-component covariance modelling

As discussed in section I the assumption that independent underlying scattering mechanisms generate independent radar backscatter components with Gaussian shaped spectra leads to a straightforward approach for the derivation of the combined covariance matrix per the developments of sections II and III. For instance, if two backscatter mechanisms are present with spectral characteristics $[\omega_{m_1}, \sigma_{c_1}]$ and $[\omega_{m_2}, \sigma_{c_2}]$, respectively, then the component covariance matrices $\mathbf{R}_{\mathbf{t},\mathbf{d}}\{1\}$ and $\mathbf{R}_{\mathbf{t},\mathbf{d}}\{2\}$ can be calculated per the approach of sections II or III. The overall clutter covariance matrix is then given by

$$\mathbf{R}_{\mathbf{t},\mathbf{d}} = P_1\mathbf{R}_{\mathbf{t},\mathbf{d}}\{1\} + P_2\mathbf{R}_{\mathbf{t},\mathbf{d}}\{2\} \tag{27}$$

where P_1 and P_2 represent the total clutter backscatter power of the first and second clutter component, respectively, and it is assumed that component covariance matrices have been previously normalised to unit power. The clutter-plus-noise covariance matrix is computed as

$$\mathbf{R} = \mathbf{R}_{\mathbf{t},\mathbf{d}} + P_{\text{noise}}\mathbf{I} \tag{28}$$

as clutter and noise are independent from each other. The matrix $\mathbf{I}$ denotes the identity matrix and P_{noise} is the noise power.

It is of some interest to brief y examine the effect of dual component models on eigenvalue behaviour. For ground clutter applications, typical modelled and measured eigenvalue spectra tend to be symmetric with peaks centred at the same Doppler velocity. In contrast sea clutter eigenspectra are frequently observed to be asymmetric with Doppler velocity offsets between different eigenvalues, see for interest [5], [7], [8], [13]. The following analysis provides some insight into the origins of this observed phenomena and, hopefully, increases the reader's physical understanding.

Figure 4 presents the post-Doppler eigenvalue spectra for covariance matrices derived from unequal and equal power component matrices with identical spectral widths. In particular the left column corresponds to the case where $\mathbf{R_{t,d}}\{2\}$ has twice the mean power of $\mathbf{R_{t,d}}\{1\}$, i.e., +3 dB, with the $\mathbf{R_{t,d}}\{1\}$ centre Doppler velocity equal to 0 m/s and the $\mathbf{R_{t,d}}\{2\}$ centre Doppler velocity equal to 1.5 m/s and 3.5 m/s, respectively, from top to bottom. Both component matrices have an associated spectral FHWM of 1.0 m/s where $2.355\sigma_c \approx$ FHWM. The right hand column of f gure 4 presents results for similar parameters with the sole exception that $\mathbf{R_{t,d}}\{1\}$ and $\mathbf{R_{t,d}}\{2\}$ have identical mean power. Examining subplot (a) of f gure 4 we note that the presence of two offset underlying Gaussian spectra with different power levels leads to a misalignment in the peaks of the eigenvalue spectra. In particular, the second eigenvalue peak occurs at a lower velocity than the f rst eigenvalue. If the relative power of the component matrices were switched (i.e. $\mathbf{R_{t,d}}\{1\}$ has twice the power of $\mathbf{R_{t,d}}\{2\}$) then the second eigenvalue peak will occur at a higher velocity than the f rst eigenvalue peak (not shown for conciseness). In contrast it can be seen in subplot (c) of f gure 4 that that peaks of the eigenvalue spectrum remain aligned when the component matrices have equal power. Gracheva [13] noted a similar offset between eigenvalue peaks in a PAMIR data set that was examined and speculated that it was due to breaking wave phenomena. Whatever the physical source, it is apparent that offsets between eigenvalue spectra peaks arise due to the presence of offset spectral components with unequal power.

To better understand this effect it is helpful to examine the angular distribution of the power response within individual Doppler bins. Figure 5 presents a plot of the 2D angle versus Doppler velocity power backscatter response that would arise for the parameters corresponding to the left hand column of f gure 4. It is apparent from f gure 5 that the ratio of the contributions from the different components varies as a function of Doppler velocity. This variation arises due to the well known effect of Doppler broadening and has been previously discussed in more detail for dual component sea clutter by McDonald and Cerutti-Maori [5]. Figure 6(a) presents the power versus angle slice from this f gure for Doppler velocity 1.12 m/s which corresponds to peak of the dominant eigenvalue in f gure 4(a). Figure 6(b) presents the projection of the eigenvectors corresponding to this Doppler bin onto angular space (i.e., angle axis). Each response has been weighted by the corresponding eigenvalue. It can be seen that the dominant eigenvector response is approximately centred on the composite angular spectrum response with a slight offset towards the global maximum spectral peak. This observation simply ref ects the fact that the primary eigenvector aligns with the coordinate in the clutter subspace which maximises its power. In contrast the second and third eigenvectors can be seen to be more heavily weighted towards the fringes of the angular spectral response.

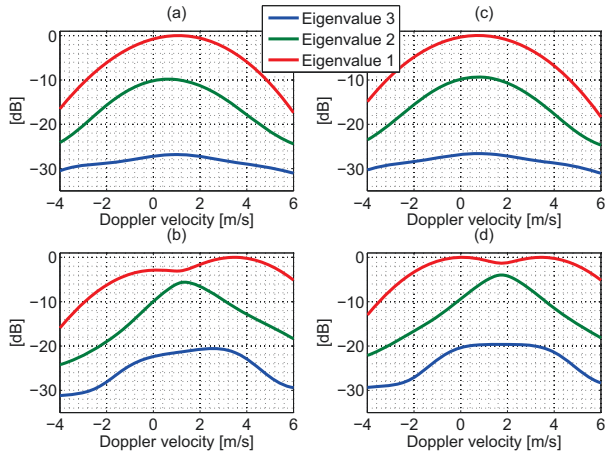

Fig. 4. Eigenvalue spectra for two-component spectral models. (a) $\mathbf{R_{t,d}}\{1\}$ centre Doppler velocity is 0 m/s, $\mathbf{R_{t,d}}\{2\}$ centre Doppler velocity is 1.5 m/s, $\frac{P_2}{P_1}$ = 2. (b) $\mathbf{R_{t,d}}\{1\}$ centre Doppler velocity is 0 m/s, $\mathbf{R_{t,d}}\{2\}$ centre Doppler velocity is 3.5 m/s, $\frac{P_2}{P_1}$ = 2. (c) $\mathbf{R_{t,d}}\{1\}$ centre Doppler velocity is 0 m/s, $\mathbf{R_{t,d}}\{2\}$ centre Doppler velocity is 1.5 m/s, $\frac{P_2}{P_1}$ = 1. (d) $\mathbf{R_{t,d}}\{1\}$ centre Doppler velocity is 0 m/s, $\mathbf{R_{t,d}}\{2\}$ centre Doppler velocity is 3.5 m/s, $\frac{P_2}{P_1}$ = 1 .

Fig. 5. Angle versus Doppler velocity backscatter response for $\mathbf{R_{t,d}}\{1\}$ centre Doppler velocity = 0 m/s, $\mathbf{R_{t,d}}\{2\}$ centre Doppler velocity = 1.5 m/s, $\frac{P_2}{P_1}$ = 2 and spectral FWHM of 1.5 m/s for both components.

This observation suggests that broader composite angular spectral responses may be associated with increases in second and third eigenvalues.

To examine this effect we calculate a measure of the angular spread of the spectrum in each Doppler bin. In particular we calculate the angular 'variance' of the spectrum in each Doppler bin as

$$\sigma^2 = \sum_{\theta} \theta^2 P_{\text{ang}}(\theta) - (\sum_{\theta} \theta P_{\text{ang}}(\theta))^2 \tag{29}$$

where P_{ang} is the spectral power for a given angle θ and σ^2 is plotted versus Doppler velocity in f gure 7(b). It can be seen that the peak variance occurs near -0.2 m/s which, although displaced in the correct direction from the peak of the primary eigenvalue, is not a particulary close match to the observed peak of the second eigenvalue at

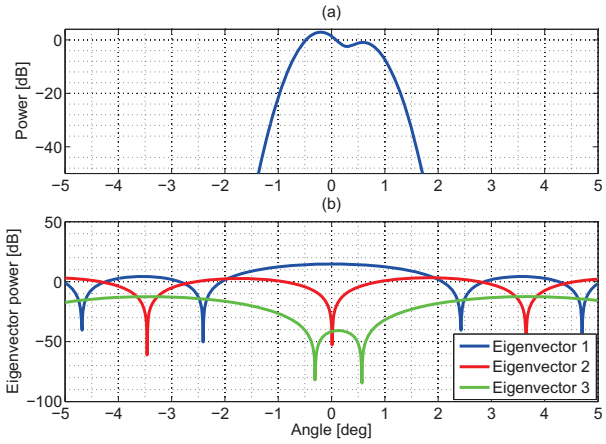

Fig. 6. (a) Power versus azimuth angle for 1.1 m/s Doppler velocity. (b) Projection of eigenvectors response onto azimuth angle. Each eigenvector projection is weighted by associated eigenvalue.

0.64 m/s. On further thought, however, it is apparent that the location of the peak of the second eigenvalue will not only be a function of the spread of the angular spectrum but will also depend on the variation of overall power response with Doppler velocity. Figure 7(a) presents the power versus Doppler velocity in which it can be seen that power is locally increasing with Doppler velocity in the region of the second eigenvalue peak. An approximate measure of the second eigenvalue tendencies, $\sigma^2 P_{\text{ang}}$, is therefore plotted in f gure 7(c) where the peak value of this product can be seen to closely align with the second eigenvalue peak in f gure7(a). This result is intuitively satisfying as it tells us that the second eigenvalue will be increased in regions where the angular clutter spectrum is broader and clutter power is large. Similar plots for the case where composite matrices have equal power (not shown for conciseness) reveal that the peaks for σ^2 and P_{ang} coincide, consistent with the fact that no displacement of the eigenvalue spectra peaks is observed despite the fact that two Gaussian spectra components are present.

As discussed above, subplots (b) and (d) of f gure 4 correspond to the case in which the centre Doppler velocity associated with each matrix component is separated by 3.5 m/s in contrast with the 1.5 m/s results discussed above. From the bimodal response of the f rst eigenvalue in these f gures it can be seen that composite spectral components are beginning to be separately resolved in the eigenspace. Figure 8 presents the plot of P_{ang} and projected eigenvector responses for the Doppler velocity bin corresponding to the f rst eigenvalue peak at 3.48 m/s in f gure 4. A similar relationship to f gure 6 is observed with the exception that the f rst eigenvector is strongly centred on the peak spectral component, i.e., the peak component is resolved within the eigenspace. Figure 9 again examines the P_{ang} and σ^2 dependencies. The peak of the $P_{\text{ang}}\sigma^2$ plot can be seen to again align quite closely with the second eigenvalue peak of 1.37 m/s in subplot (c) of f gure 4. As discussed by McDonald and Cerutti-Maori [7], the ability of the eigenvector basis to resolve spectral components in angle is a function of the total antenna azimuth width. Therefore a similar separation of responses could have been achieved by increasing the antenna width rather than increasing the spectral separation. Furthermore, under conditions of greater spectral separation (or increased azimuth resolution)

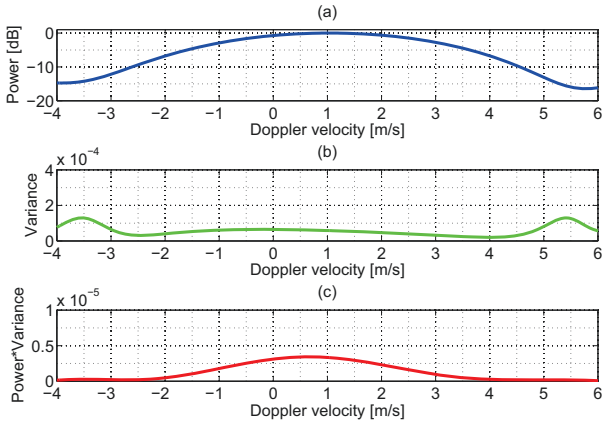

Fig. 7. Spectral characteristics for $\mathbf{R}_{\mathbf{t},\mathbf{d}}\{1\}$ centre Doppler velocity = 0 m/s, $\mathbf{R}_{\mathbf{t},\mathbf{d}}\{2\}$ centre Doppler velocity = 1.5 m/s, $\frac{P_2}{P_1}$ = 2 and spectral FWHM of 1.5 m/s for both components. (a) Power versus Doppler velocity.(b) Measure of spectral angular width (variance) versus Doppler velocity. (c) Power$\times$Variance versus Doppler velocity.

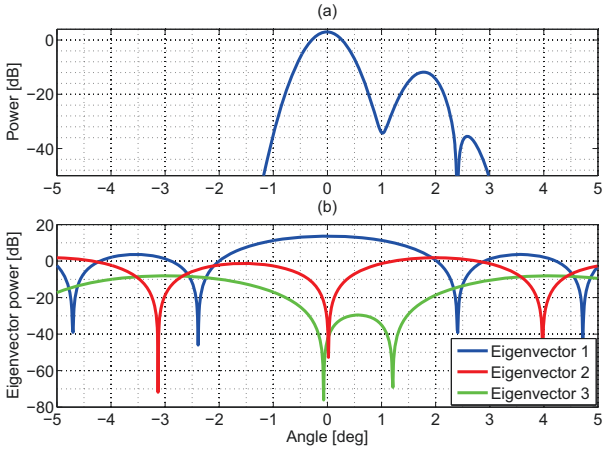

Fig. 8. (a) Power versus azimuth angle for 3.5 m/s Doppler velocity. (b) Projection of eigenvectors response onto azimuth angle. Each eigenvector projection is weighted by associated eigenvalue.

the second eigenvalue response can be observed to develop local maximums coincident with the first eigenvalues spectra peaks (not shown for conciseness) and in the limit of very large frequency separation or very fine angular resolution (which may not be realisable in a practical system) the intermediate global maximum eigenvalue peak would be expected to vanish.

V. Conclusion

The closed form expressions presented in this paper provide accurate models for predicting the clairvoyant covariance matrix corresponding to radar sea clutter backscatter comprised of backscatter responses corresponding

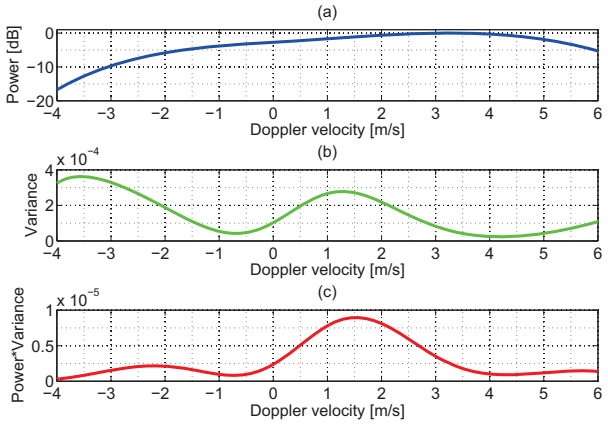

Fig. 9. Spectral characteristics for $\mathbf{R_{t,d}}\{1\}$ centre Doppler velocity = 0 m/s, $\mathbf{R_{t,d}}\{2\}$ centre Doppler velocity = 3.5 m/s, $\frac{P_2}{P_1}$ = 2 and spectral FWHM of $1.5m/s$ for both components (a) Power versus Doppler velocity.(b) Measure of spectral angular width (variance) versus Doppler velocity. (c) Power$\times$Variance versus Doppler velocity.

to Gaussian shaped spectra. The ability to combine Gaussian spectra allows for overall clutter spectra to be closely replicated to arbitrary accuracy. The results have utility for the eff cient simulation of data as they provide a method for direct calculation of the clairvoyant covariance matrix which can then be used to generate backscatter realisations (for example, the Cholesky decomposition of the clairvoyant matrix followed by multiplication with a complex normal measurement vector) without the need to generate an initial estimate of the covariance matrix via simulated data. The resulting closed form clairvoyant matrix allows for direct calculation of the eigenvalue decomposition which would arise from arbitrary Gaussian spectral components.

Although the assumption of underlying Gaussian spectral components has been shown to reasonably capture broad characteristics of observed eigenspectra behaviour,see for interest [5], [7], [8], [13], a word of caution is warranted. Since covariance matrices are, by def nition, second moment functions they are not capable of directly capturing and conveying information about differences in statistical behaviour, such as different spikiness, between composite clutter components. The most common approach to estimating a covariance matrix estimate in a real world system is to form the sample covariance matrix (SCM) as follow

$$\widehat{\mathbf{R}}_{\text{SCM}} = \sum_{r=1}^{N_{bs}} \mathbf{Z}_r \mathbf{Z}_r^H \tag{30}$$

where N_{bs} is the number of background samples of the signal vector, $\mathbf{Z}_r$ (typically taken from each range sample r), used in the estimation. Given the above formulation, $\widehat{\mathbf{R}}_{\text{SCM}}$ only provides insights into the mean power of each component across the background sample size. Furthermore the limited number of background samples that are available to estimate the SCM (due to system limitations and spatial nonhomogeneity of clutter) will lead to statistical variations of SCM estimates with respect to the clairvoyant covariance matrix. These variations will be highly sensitive to the spikeiness of clutter backscatter responses and is a topic of ongoing study. As discussed by McDonald and Cerutti-Maori [7], f uctuations of component powers on a range cell to range cell basis can have a

signif cant impact on constant false alarm rate (CFAR) performance and cannot be predicted or simulated on the basis of the $\widehat{\mathbf{R}}_{\text{SCM}}$ (or equivalently variations of signal-to-clutter-plus-noise ratio (SCNR)) alone. Nevertheless the closed form approach presented above will allow the calculation of accurate estimates of $\widehat{\mathbf{R}}_{\text{SCM}}$ in the case where mean component powers are known. Furthermore if the expected f uctuation of spectral parameters is known a priori it is relatively simple and computationally eff cient to calculate different clairvoyant covariance matrices for individual realisations, e.g., on a range cell to range cell, or CPI by CPI basis.

REFERENCES

[1] D. Walker, "Experimentally motivated model for low grazing angle radar doppler spectra of the sea surface," IEE Proc F, Radar Sonar Navig., vol. 147, no. 3, pp. 114–120, 2000.

[2] ——, "Doppler modelling of radar sea clutter," Radar, Sonar and Navigation, IEE Proceedings -, vol. 148, no. 2, pp. 73–80, Apr 2001.

[3] T. Lamont-Smith, K. Ward, and D. Walker, "A comparison of em scattering results and radar sea clutter," in RADAR 2002, Oct. 2002, pp. 439–443.

[4] P. Lee, J. Barter, B. Lake, and H. Thompson, "Lineshape analysis of breaking-wave doppler spectra," Radar, Sonar and Navigation, IEE Proceedings -, vol. 145, no. 2, pp. 135–139, Apr 1998.

[5] M. McDonald and D. Cerutti-Maori, "Coherent radar processing in sea clutter environments part 1," in press IEEE Transactions on Aerospace and Electronic Systems.

[6] M. McDonald and D.Cerutti-Maori, "Statistical and spectral modelling of medium grazing angle coherent radar data," in 2015 IEEE Radar Conference Symposium Proceedings.

[7] M. McDonald and D. Cerutti-Maori, "Coherent radar processing in sea clutter environments part 2," in press IEEE Transactions on Aerospace and Electronic Systems.

[8] M. Mcdonald, D. Cerutti-Maori, and A. Damini, "Characterisation and cancellation of medium grazing angle sea clutter," in Radar Conference (EuRAD), 2010 European, 2010, pp. 172–175.

[9] M. McDonald and D.Cerutti-Maori, "Adaptive normalised matched f lter performance in medium grazing angle sea clutter," in submitted to 2015 IEEE Radar Conference.

[10] V. Zavorotny and A. Voronovich, "Two-scale model and ocean radar doppler spectra at moderate- and low-grazing angles," Antennas and Propagation, IEEE Transactions on, vol. 46, no. 1, pp. 84–92, 1998.

[11] J. Ward, "Space-time adaptive processing for airborne radar," in Space-Time Adaptive Processing (Ref. No. 1998/241), IEE Colloquium on, 1998, pp. 2/1–2/6.

[12] V. Gracheva and J. Ender, "Multichannel analysis of medium grazing angle sea clutter," in EUSAR 2014; 10th European Conference on Synthetic Aperture Radar; Proceedings of, June 2014, pp. 1–4.

[13] ——, "Eigenvalue analysis of airborne multichannel sea data for ocean monitoring," in press EUSAR 2016, 2016.